

Determination of the Orbital Elements of PHA 1998 OH via the Method of Gauss

Elias Finkelstein, Ryan LoRusso, and Irene Xu

Summer Science Program, New Mexico Tech

20 July 2019

Abstract. Near-earth asteroids have been tracked for decades in attempt to prevent a potentially destructive impact on the Earth. The asteroid 1998 OH, one of 1,500 potentially hazardous asteroids, was observed for several weeks in order to calculate its positional coordinates with astrometry, determine its six orbital elements using the Method of Gauss, and characterize its orbit. After calculating the orbital elements, improving its accuracy, and determining the uncertainties of the elements through comparisons with H. Butler, K. Kang, and S. Tangs' data as well as Monte Carlo simulations, the positional data and orbital elements can be used to confirm the orbit of 1998 OH.

1 Introduction

On July 19, 1998, Apollo class asteroid 12538 (temporary designation 1998 OH) was discovered at Haleakalā Observatory, Hawaii [1]. Because discovering an asteroid is not an uncommon occurrence, it is not always a concerning one. 1998 OH was an exception. As a potentially hazardous asteroid (PHA) [2], a class of asteroids with orbits that come within 0.05 AU of the Earth and have a diameter larger than 140 meters [3], 1998 OH was a somewhat concerning find. At closest approach, 1998 OH is only 0.0287 AU from the Earth and its diameter is 1.6 kilometers, far within the margins of a PHA. Although most PHAs are not predicted to hit the Earth, slight perturbations to their orbits from the gravity of other planets or collisions with foreign objects could shift them onto an intercepting path. For this reason, it is important to observe PHAs regularly to ensure that their orbits have not been disturbed.

To give some perspective on what an asteroid impact would do, it is useful to reference the Chelyabinsk meteor that entered Earth's atmosphere in early 2013. As the meteor plummeted to the Earth, it was visible in hundreds of dash cams across the city and even though the meteor exploded in midair without contacting the ground, the energy released was equivalent to approximately 25 Hiroshima atomic bombs, shattering thousands of windows and sending over 1,500 people to seek medical attention for various injuries [4]. The Chelyabinsk meteor was only 20 meters wide whereas the average PHA as stated above is over 140 meters. A PHA impacting the Earth would therefore cause mass destruction.

Vigilant observation of PHAs could give us an opportunity to prepare for an asteroid impact. With enough warning, an impact could be avoided altogether. By 2021, NASA plans to attempt their Double Asteroid Redirection Test (DART), which is expected to demonstrate “the kinetic impact technique to deflect an asteroid” [5]. Other proposals deflect asteroids have been presented, but none of these solutions can be enacted without adequate warning.

Therefore, accurate orbital information must be calculated constantly to understand the object's position and velocity in relation to Earth. The first method for orbital determination was proposed by Carl Friedrich Gauss in 1801 [6]. The Method of Gauss, which was originally used on the asteroid Ceres, centers around three observations on three separate nights to measure the position and velocity vectors of an orbiting object.

Over the course of five weeks, seven observations of PHA 1998 OH were attempted at Etsorn Observatory in Socorro, New Mexico. The purpose of these observations was to obtain positional data for 1998 OH on at least three different nights in order to calculate orbital information using the Method of Gauss. Of the seven attempted observations, only four were usable. Although 1998 OH is a well documented asteroid, the methods explored in this paper can be applied to all types of near-Earth asteroids.

2 Materials and Methodology

2.1 Instruments and Software

All observations of 1998 OH took place at Etsorn Observatory (MPC designation 719) in Socorro, New Mexico. The C-14 Telescope at the Etsorn, which has a 22x32 arc-minute field of view, was used to take images of 1998 OH during four of the seven observation sessions and to collect data for cloudy

night experiments during the other three observation sessions.

Two pieces of software were used to process astronomical images. The first, AstroImageJ (AIJ), was used for dark subtraction, bias subtraction, and flat division of the raw image data. These three operations corrected for much of the instrumental error such as vignetting, noise, and dust on the CCD chip. AstroImageJ was further used to align all images from an observation such that the movement of the asteroid could be confirmed. The second piece of software, DS9, was used in astrometry and photometry. These two processes were responsible for obtaining approximations for the equatorial coordinates and apparent visual magnitude of the asteroid for each observation.

2.1.1 Pre-Observation Routines

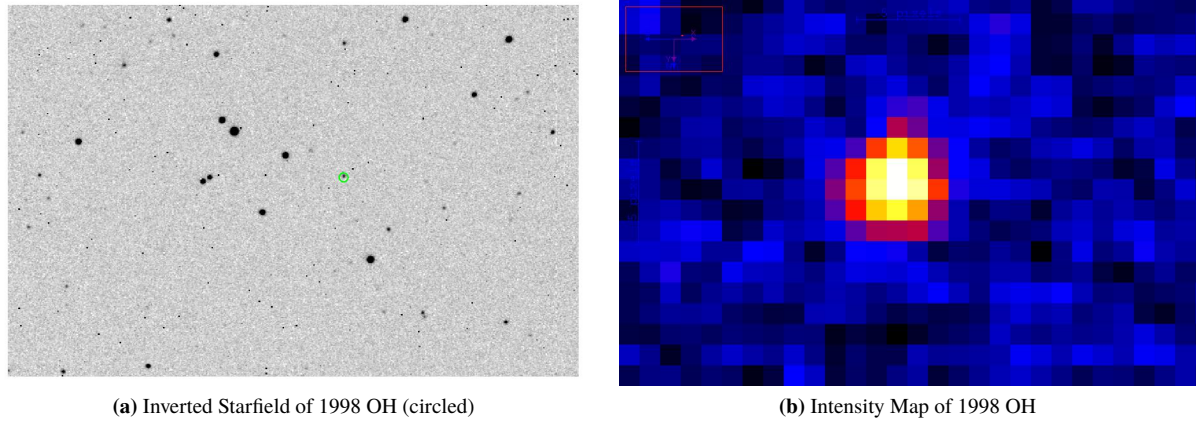
Before undertaking each observation, preparation went into ensuring an efficient and productive session. First, an ephemeris was printed from JPL Horizons to obtain positional data for the asteroid. The ephemeris also included the apparent magnitude of the asteroid, the brightness of the moon, and angle to the moon, which could be taken into account when considering exposure times. A star chart was printed from DS9 to plot the predicted equatorial coordinates from the ephemeris in order to anticipate the asteroid's path. This was used during and after observation to ensure that the telescope had slewed to the right location and to help with finding the asteroid. A focus star between the visual magnitudes of three and six was found using the Yale Bright Star Catalogue from DS9 to help ensure a sharp image.

2.2 Observations

2.2.1 Observation Strategy

Upon arriving at Etscorn, the telescope was slewed to the focus star, a Bahtinov mask was placed in front of the telescope opening, and the CCD chip was cooled to -10°C . After taking three to four test exposures and adjusting the focus accordingly, the Bahtinov mask would be taken off and the telescope would be slewed to the asteroid. From there, the telescope would track the same predicted equatorial coordinates from JPL Horizons until two or three series of exposures had been taken, with a standard length of 11 images per series (sometimes shortened due to lack of remaining observation time). These exposures would take approximately 1.5 hours. The resulting images were downloaded onto a flash drive and were processed the next day using DS9 and AIJ.

During observation, it was also important to take darks and biases which were used later in image processing. Darks are taken with the same exposure time and camera settings as the original images with the shutter closed instead of open. The purpose of darks is to capture the noise created due to the thermal energy of the camera. These are subtracted from the final image to get rid of this noise. The biases are taken with no exposure time and are also subtracted from the final image to get rid of any noise inherent in the camera. Flats were taken weekly against the inside of the telescope dome with the lights on. These were divided out of the final images to reduce the dust spots or vignetting. For instance, the inverted image of one of the reduced images using AstroImageJ is shown in Figure 1, from which 1998 OH was spotted. Then, from the image, the asteroid was analyzed. For instance, after the asteroid was identified, an intensity color scale was created using the DS9 software, which depicts the decreasing signal levels from the center of the asteroid to the surrounding noise.

**Figure 1:** Finding 1998 OH

As shown in Table 1, observations took place between 9:00 pm and 3:00 am. Conditions varied significantly from night to night. The first two observations saw high quality conditions with little to no cloud coverage, whereas the last five saw intermittent and at times complete cloud coverage. Due to the range of observation times, 1998 OH was at lower altitudes for some nights and higher for others, which contributed to fluctuations in seeing, the quality of a given image as a result of atmospheric density. In addition to unpredictable weather patterns and seeing, the apparent visual magnitude of 1998 OH increased steadily over the course of the five weeks of observations. Exposure times began at 90 seconds, but were forced up to 120 seconds by week three as the asteroid got dimmer. Observation 3 was particularly cloudy, and the filter was changed to clear, unlike the other nights where a visual filter was used.

Table 1: Observation Sessions Data

Obs.	Date (UTC)	RA (hh:mm:ss)	Dec ($^{\circ}$ ' ")	Filter	Exp. Time	Images	Image Qual.
1	Jun 21 5:00-7:00	14 40 21.50	+37 05 39.3	Green	60/90 s	22	observable
2	Jun 26 5:00-7:00	14 58 34.16	+35 24 20.3	Green	90 s	27	observable
A*	Jun 29 7:00-9:00	15 08 21.66	+34 19 59.2	Dark	N/A	N/A	not observable
B*	Jul 3 7:00-9:00	15 19 51.10	+32 55 21.9	Dark	N/A	N/A	not observable
C*	Jul 8 5:00-7:00	15 32 33.06	+31 10 24.6	Bias	N/A	N/A	not observable
3	Jul 11 5:00-7:00	15 39 42.41	+30 06 11.4	Clear	120 s	22	**observable
4	Jul 15 5:00-7:00	15 48 42.88	+28 40 42.7	Green	120 s	33	**observable

*denotes cloudy night experiments

**denotes that the asteroid was observable but partial cloud coverage may affect the quality of some of the images

3 Data and Analysis

3.1 Analyzing the Raw Data

Before analyzing raw data, it is important to use a universal coordinate system. The equatorial coordinate system, which isn't location dependent, is used by astronomers to refer to locations of objects in the sky. This coordinate system, denoted by right ascension (α) and declination (δ), uses the equatorial plane of the Earth as a reference point and the Vernal Equinox as a zero point ($\alpha = 0$, $\delta = 0$). The position of objects is mapped onto a geocentric celestial sphere. Right ascension uses great circle lines passing through both celestial poles to measure the East-West position of an object in the sky. Declination, on the other hand, uses circular lines parallel to the celestial equator to measure the North-South position of an object in the sky. Together, right ascension and declination can refer to any location on the celestial sphere. [7]

3.1.1 Astrometry

The first and most important step in obtaining positional data from astronomical images is astrometry, which is the process by which image data in the form of x and y pixel coordinates are transformed into equatorial coordinates in order to provide accurate positional information for 1998 OH. To determine accurate relationships between equatorial and pixel coordinates, approximately ten reference stars with known positional data are needed. Equatorial coordinates of stars are well cataloged in numerous databases (GAIA DR2 was used during this research process) and comparing the positional data from these databases to the pixel coordinates in the astronomical images gives a relationship between the two.

The best way to determine this relationship is with a Least Squares Plate Reduction, abbreviated as LSPR. The LSPR method takes in known relationships as inputs and then outputs six plate constants: b_1 , b_2 , a_{11} , a_{12} , a_{21} , and a_{22} . As shown in the equations below, the plate constants are calculated using the positional data of the reference stars, where the sums $i = 1$ to $i = N$ are taken for the Cartesian and positional coordinates.

$$\begin{pmatrix} \sum \alpha_i \\ \sum \alpha_i x_i \\ \sum \alpha_i y_i \end{pmatrix} = \begin{pmatrix} N & \sum x_i & \sum y_i \\ \sum x_i & \sum (x_i)^2 & \sum x_i y_i \\ \sum y_i & \sum x_i y_i & \sum (y_i)^2 \end{pmatrix} \begin{pmatrix} b_1 \\ a_{11} \\ a_{12} \end{pmatrix}$$

$$\begin{pmatrix} \sum \delta_i \\ \sum \delta_i x_i \\ \sum \delta_i y_i \end{pmatrix} = \begin{pmatrix} N & \sum x_i & \sum y_i \\ \sum x_i & \sum (x_i)^2 & \sum x_i y_i \\ \sum y_i & \sum x_i y_i & \sum (y_i)^2 \end{pmatrix} \begin{pmatrix} b_2 \\ a_{21} \\ a_{22} \end{pmatrix}$$

These equations can then be used to convert the Cartesian coordinates of the asteroid into equatorial coordinates using the equations below, where the x and y values refer to the pixel positions in the reduced and aligned images obtained with AstroImageJ.

$$\alpha = b_1 + a_{11}x + a_{12}y$$

$$\delta = b_2 + a_{21}x + a_{22}y$$

LSPR gets more complicated, however, because the pixel coordinate plane is two-dimensional whereas the equatorial coordinate system is three-dimensional. Although the curvature of this spherical surface

is incredibly small in the field of view of the telescope, it must be taken into account while calculating plate constants. To deal with the curvature of the equatorial coordinate system, it is temporarily “flattened” and a relationship is determined between the flattened plane and the pixel coordinates. New “flat α ” and “flat δ ” are calculated and then “unflattened” to reflect corresponding coordinates in the original equatorial coordinate system. This correction is small, but necessary to obtain accurate astrometry.

To calculate uncertainty of the equatorial coordinates, the code is run again with the x and y coordinates of the stars initially used to calculate the plate constants. The resulting right ascension and declination are then compared against the known values and the difference is taken. The equation below is then used to get the uncertainty of the calculated values, where N represents the total number of stars used to conduct the astrometry and the uncertainty units are arcseconds.

$$\sigma_{\alpha} = \sqrt{\frac{1}{N-3} \sum \alpha_{real} - \alpha_{fit}}$$

$$\sigma_{\delta} = \sqrt{\frac{1}{N-3} \sum \delta_{real} - \delta_{fit}}$$

Furthermore, the positional coordinates calculated for the asteroid were all within a single arcsecond of uncertainty as shown in the following table. These results were then later used to calculate the positional and velocity vectors of 1998 OH through the Method of Gauss and again, used in differential correction to determine the deviations between the calculated fit coordinates and the observed coordinates.

Table 2: Resulting RAs (α) and Decs (δ) of 1998 OH from Astrometry

Obs.	Date (UTC)	α (hh:mm:ss)	σ_{α} (s)	δ ($^{\circ}$ ' ")	σ_{δ} (")
1	Jun 21 5:00-7:00	14 40 28.65	$\pm.75$	37 05 01.1	$\pm.20$
2	Jun 26 5:00-7:00	14 58 32.21	$\pm.28$	35 24 33.4	$\pm.28$
3	Jul 11 5:00-7:00	15 39 38.74	$\pm.37$	30 06 47.3	$\pm.27$
4	Jul 15 5:00-7:00	15 48 43.94	$\pm.31$	28 40 31.6	$\pm.26$

3.1.2 Photometry

Like astrometry, photometry compares values from both an image and a database, which the method then uses to determine a relationship between instrumental and visual magnitude, which can then be used to calculate the relative size and rotation rate of the asteroid. Obtaining photometric data begins with calculating the relative brightness of the stars in an image. Like astrometry, the known objects are stars, whose apparent visual magnitudes are well documented. Comparing a relative brightness with a visual magnitude gives a reliable relationship between instrumental and visual magnitudes that can then be used to determine the visual magnitude of the asteroid.

The relative brightness of objects is calculated using aperture photometry, a process that returns an instrumental magnitude for a specified aperture and annulus in an image. An aperture is a circle of a given radius centered on a region of interest. An annulus is also centered on the region of interest, but creates a ring of pixels around the center instead, which provide the average sky value around the object.

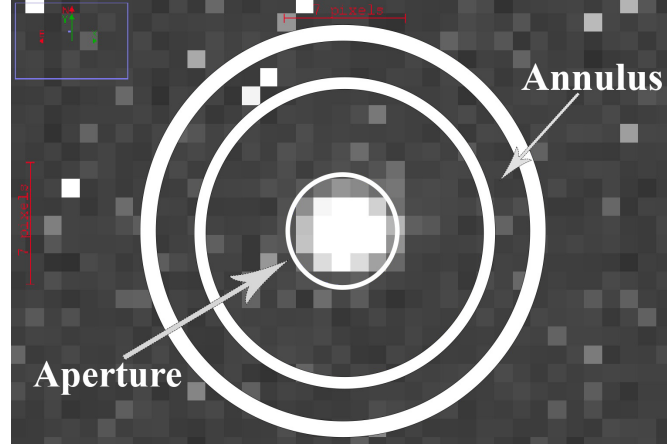


Figure 2: Visual of an Aperture and an Annulus of 1998 OH

Because pixels are square in shape, it is difficult to obtain a good approximation of a circle, especially when the region of interest becomes very small. 1998 OH, which is approximately six pixels wide using the C14 telescope at Etsorn, is hardly wide enough to create an accurate representation of a circle with the aperture. To combat this inaccuracy, the signal value of pixels was weighted corresponding to the fraction of a given pixel within the circle. The pixels in the image, under this modification, were then used to determine the average signal of the pixels.

Together, the aperture and annulus are used to calculate the overall signal from the region of interest and the signal to noise ratio (SNR). The signal (S) is the sum of all pixel counts from the aperture subtracted by an average sky value (Sky_{e^-}). The SNR, on the other hand, is the ratio of signal to the total uncertainty, noise (N) in an image. SNR and signal are then used to calculate an instrumental magnitude for the region inside the aperture. The instrumental magnitude acts as a relative brightness that can be compared with all other parts of the same image. While describing the SNR as a ratio of signal and noise sounds simple in theory, the equation to determine the SNR requires other values, including the number of pixels in the aperture (n_{ap}), the number of pixels in the annulus (n_{an}), the dark current (D_e), and the electronic read noise (ρ). Additionally, to maintain consistency in the values' units, signal is in terms of e^- and Sky_{e^-} and D_e are in terms of $\frac{e^-}{pixel}$, which requires unit conversions from the units of ADU and $\frac{ADU}{pixel}$ respectively by multiply each term by the gain of the camera.

$$SNR = \frac{S}{N} = \frac{\sqrt{S}}{\sqrt{(1 + n_{ap}(1 + \frac{n_{ap}}{n_{an}})(\frac{Sky_{e^-} + D_e + \rho^2}{S})}}}$$

$$\rho^2 = read^2 + \frac{gain^2}{12}$$

Through aperture photometry, the uncertainty of the calculated instrumental magnitudes are determined by the equation below:

$$\sigma = \frac{1.0875}{SNR}$$

After calculating the instrumental magnitudes and collecting the apparent visual magnitudes of seven to ten stars, a line of best fit can be calculated to give a linear relationship between the two. The instrumental magnitude of the the asteroid can then be calculated and graphed on the line, resulting in an approximate apparent visual magnitude.

Table 3: Resulting Instrumental and Visual Magnitudes of 1998 OH from Aperture Photometry

Obs.	Date (UTC)	$Mag_{(Inst)}$	σ_{Inst}	$VMag$
1	Jun 21 5:00-7:00	-8.645	$\pm.06$	16.42
2	Jun 26 5:00-7:00	-8.198	$\pm.07$	16.80
3	Jul 11 5:00-7:00	-8.970	$\pm.08$	17.16
4	Jul 15 5:00-7:00	-7.713	$\pm.23$	17.56

3.2 \vec{r} and $\dot{\vec{r}}$

In this and the following sections on the determination of orbital elements and the Method of Gauss, unless otherwise stated, all equations and methodologies are drawn from the one reference listed here [8].

While astrometry gives values for right ascension and declination, there is a major issue with the positional data collected so far—there is no indication as to the asteroid’s distance from the Earth. This is the most critical value to be found.

The positional relationship between the Earth, the sun, and a given body can be described by three vectors: \vec{r} , \vec{R} , and $\vec{\rho}$. \vec{r} represents the vector drawn from the sun to the given body, \vec{R} represents the vector drawn from the Earth to the sun, and $\vec{\rho}$ represents the vector drawn from the Earth to the given body. According to spherical trigonometry, the direction of $\vec{\rho}$ — $\hat{\rho}$ —can be determined from a given right ascension and declination according to the following equation.

$$\hat{\rho} = (\cos \alpha \cos \delta)\hat{i} + (\sin \alpha \cos \delta)\hat{j} + (\sin \alpha)\hat{k}$$

where α is right ascension, δ is declination, and $\hat{i}, \hat{j}, \hat{k}$ are basis vectors. For the purposes of this research, it is assumed that \vec{R} is known for all observations. Since the goal of the research is to determine orbital elements for a given body, and the orbital elements are in large part calculated from \vec{r} and $\dot{\vec{r}}$, that is the unknown which must be solved for. By vector arithmetic based upon the physical descriptions of \vec{r} , \vec{R} , and $\vec{\rho}$, the following can be stated.

$$\vec{r} = \vec{\rho} - \vec{R}$$

$$\dot{\vec{r}} = \dot{\vec{\rho}} - \dot{\vec{R}}$$

In this way a direct relationship between the other two vectors and \vec{r} has been created. And as $\hat{\rho}$ and \vec{R} are known, that leaves ρ as the component which needs be inputted into these equations. By splitting $\vec{\rho}$ into ρ and $\hat{\rho}$, \vec{r} and $\dot{\vec{r}}$ can be described by the equations

$$\vec{r} = \rho\hat{\rho} - \vec{R}$$

$$\dot{\vec{r}} = \dot{\rho}\hat{\rho} + \rho\dot{\hat{\rho}} - \dot{\vec{R}}$$

Additionally, the orientation of the orbit in three-dimensional space can be found from the cross product of \vec{r} and $\dot{\vec{r}}$. By evaluating that relationship, it can be determined that

$$\vec{h} = (\vec{r} \times \dot{\vec{r}})$$

where \vec{h} is the vector representing angular momentum per unit mass. Because the vectors \vec{r} and $\dot{\vec{r}}$ are both contained within the orbital plane, and \vec{h} is their cross product, the direction of \vec{h} must describe how the orbital plane of the body is oriented to the rest of the system.

3.3 The Orbital Elements

After determining \vec{r}_2 and $\dot{\vec{r}}_2$, it is possible to determine the orbital elements of a body. First, the semi-major axis (a), which denotes the line segment connecting the asteroid's average distance to the center of its orbit, can be calculated with the following equation:

$$a = \left(\frac{2}{|\dot{\vec{r}}_2|^2} - \frac{\dot{\vec{r}}_2 \cdot \dot{\vec{r}}_2}{\mu} \right)^{-1}$$

where the \vec{r}_2 and $\dot{\vec{r}}_2$ vectors represent the positional and velocity vectors of 1998 OH during the time of the second out of the three observations inputted into the Method of Gauss. Additionally, μ represents the square of the Gaussian constant k .

Now, with the semi-major axis, the eccentricity (e) of the asteroid's orbit, a number that represents the deviation of the asteroid from a circular orbit, was calculated with the following equation.

$$e = \sqrt{1 - \frac{|\vec{r}_2 \times \dot{\vec{r}}_2|^2}{\mu a^3}}$$

Then, after determining two of the six orbital elements, the h plane, which is perpendicular to the orbital plane and thus, determines its orientation in space, is used to determine the inclination (i) of the asteroid's orbit; the inclination denotes the angle between the ecliptic plane and the asteroid's orbital plane. Because the angle between $|\vec{h}|$ and h_z is congruent to the inclination angle, i can be determined using the following equation:

$$\cos i = \frac{h_z}{|\vec{h}|}$$

With the orbit inclination of 1998 OH, the longitude of the ascending node (Ω), which represents the asteroid's counter-clockwise angle from the Vernal Equinox on the ecliptic plane, can be calculated. However, to prevent quadrant ambiguity, sine and cosine functions were used to determine Ω (as shown in the equation below).

$$\sin \Omega = \frac{h_x}{h \sin i}$$

$$\cos \Omega = -\frac{h_y}{h \sin i}$$

Afterwards, the argument of perihelion (ω) was calculated. This orbital element represents the distance from the ascending node to the perihelion. However, two other values are needed to calculate ω : U , the angular distance from the ascending node to the asteroid, and ν , the distance from the perihelion to the asteroid (true anomaly). While ω itself is relatively simple to calculate,

$$\omega = U - \nu$$

the components U and ν require further equations as shown below. Again, sine and cosine functions were used to eliminate quadrant ambiguity.

$$\begin{aligned} \cos U &= \frac{x \cos \Omega + y \sin \Omega}{r_2} & \sin U &= \frac{z}{r_2 \sin i} \\ \cos \nu &= \left[\frac{a(1 - e^2)}{r} - 1 \right] & \sin \nu &= \frac{a(1 - e^2)}{h} \frac{\vec{r}_2 \cdot \vec{r}_2}{r} \end{aligned}$$

Finally, the mean anomaly (M) was determined. Because this final orbital element determines the angle between the center of the elliptical orbit and the ghost asteroid, which follows a circular orbit with a radius equal to the asteroid's semi-major axis, it changes as the asteroid moves along its orbit. Hence, the mean anomaly is time dependent. Therefore, to calculate the mean anomaly for the central observation, the following equation was used:

$$M_2 = E - e \sin E$$

Other values including the eccentric anomaly, the mean motion, and the period (P) of the asteroid were calculated to better understand the orbit of 1998 OH.

Yet while \vec{r}_2 and $\dot{\vec{r}}_2$ have been defined in terms of their physical meaning, we have not determined their actual values. To determine their actual values, another, far more complex step must be added to this already involved process: the Method of Gauss.

3.4 The Method of Gauss

The Method of Gauss is a preliminary method of orbit determination for determining \vec{r} and $\dot{\vec{r}}$ based upon observational data.

The Method of Gauss requires three observations of a body and the respective observed right ascensions, declinations, and times of observation. From these inputs, the ρ of the body can be found for each observation, and thus the \vec{r} and $\dot{\vec{r}}$, where the subscripts 1, 2, and 3 indicate the first, second, and third observations, respectively. The Method of Gauss works best when a body's ρ is small; as the body observed for this orbit determination was a Near-Earth Asteroid, it is unlikely that ρ was large enough to affect the method.

In order to use the Method of Gauss, the units of time must be changed from standard time into Gaussian time, centered about the middle observation. Gaussian time is described in units of Gaussian days. For a body in a circular orbit of 1 AU about the another, the period in Gaussian days of the body

is 2π . Determination of Gaussian time can be achieved by the following set of equations,

$$\tau_3 = k(t_3 - t_2)$$

$$\tau_1 = k(t_1 - t_2)$$

$$\tau = \tau_3 - \tau_1$$

where t_1 , t_2 , and t_3 are the times of observation, and k is the Gaussian constant, approximately equal to 0.01720209895 for the purposes of this system.

3.4.1 The Method

Let \vec{r}_1 and \vec{r}_3 be described in terms of \vec{r}_2 and $\dot{\vec{r}}_2$. By conservation of angular momentum, this description gives results in terms of the following equations,

$$\vec{r}_1 = f_1 \vec{r}_2 + g_1 \dot{\vec{r}}_2$$

$$\vec{r}_3 = f_3 \vec{r}_2 + g_3 \dot{\vec{r}}_2$$

where f and g are scalar functions. We can also describe \vec{r}_2 in terms of \vec{r}_1 and \vec{r}_3 . By conservation of angular momentum,

$$\vec{r}_2 = c_1 \vec{r}_1 + c_3 \vec{r}_3$$

where c_1 and c_3 are scalar constants, described by the following equations:

$$c_1 = \frac{g_3}{f_1 g_3 - g_1 f_3}$$

$$c_3 = \frac{-g_1}{f_1 g_3 - g_1 f_3}$$

In order to find \vec{r} and $\dot{\vec{r}}_2$, the ρ must be found for each observation. According to the scalar equations of range, the ρ can be described by the following series of equations.

$$\rho_1 = \frac{c_1 D_{11} + c_2 D_{12} + c_3 D_{13}}{c_1 D_o}$$

$$\rho_2 = \frac{c_1 D_{21} + c_2 D_{22} + c_3 D_{23}}{c_2 D_o}$$

$$\rho_3 = \frac{c_1 D_{31} + c_2 D_{32} + c_3 D_{33}}{c_3 D_o}$$

where the D_{ij} are constants described by the following vector equations

$$D_o = \hat{\rho}_1 \cdot (\hat{\rho}_2 \times \hat{\rho}_3)$$

$$D_{1j} = (\vec{R}_j \times \hat{\rho}_2) \cdot \hat{\rho}_3$$

$$D_{2j} = (\hat{\rho}_1 \times \vec{R}_j) \cdot \hat{\rho}_3$$

$$D_{3j} = \hat{\rho}_1 \cdot (\hat{\rho}_2 \times \vec{R}_j)$$

for a given j of 1, 2, or 3.

These scalar equations of range then result in first issue with the Method of Gauss. If the body observed shows great circle motion on the sky, then D_o will approach zero, the solutions to ρ_1 , ρ_2 , and ρ_3 will diverge, and the Method will fail.

$\dot{\vec{r}}_2$, however, has not yet been able to be determined, as the values for $\dot{\rho}$, $\dot{\hat{\rho}}$, and $\dot{\vec{R}}$ are not known and have not been shown. However, $\dot{\vec{r}}_2$ can be determined through an alternative formula,

$$\dot{\vec{r}}_2 = d_1 \vec{r}_1 + d_3 \vec{r}_3$$

where d_1 and d_3 are scalar constants, described by the following equations:

$$d_1 = \frac{-f_3}{f_1 g_3 - g_1 f_3}$$

$$d_3 = \frac{f_1}{f_1 g_3 - g_1 f_3}$$

Now, the final component is determining the values of f and g . Here, more problems start to appear. f and g are contingent upon the orbital elements, which are contingent upon \vec{r}_2 and $\dot{\vec{r}}_2$, which are contingent upon ρ_1 , ρ_2 , and ρ_3 , which are contingent upon f and g . Thus, to solve for \vec{r}_2 and $\dot{\vec{r}}_2$, the method must be iterated until it converges, if it converges at all.

For the first iteration, the expressions for f and g as well as \vec{r}_2 must be simplified. A simplified Taylor series method was used, with only the first two terms for f and g from the Taylor series used, such that neither the \vec{r}_2 vector nor the orbital elements were required for the first input. These simplified equations are as follows:

$$f_i = 1 - \frac{\mu}{2r_2^3} \tau_i^2$$

$$g_i = \tau_i - \frac{\mu}{6r_2^3} \tau_i^3$$

The reader will, notice, however, that these simplified formulas require r_2 to be an input. BUt, to guess or use predicted values from the JPL Horizons database would introduce bias into the results. As such, r_2 needs be mathematically determined via the Scalar Equation of Lagrange.

3.4.2 Scalar Equation of Lagrange

The scalar equation of Lagrange is an eighth-order polynomial equation whose real, positive roots approximate the possible r_2 values. Each value must be tested through the entire Method of Gauss. As it is an approximation, some and possibly all roots may not converge to the correct solution. The Scalar Equation of Lagrange is represented as

$$r_2^8 + ar_2^6 + br_2^3 + c = 0$$

where a , b , and c are constants described by the equations

$$\begin{aligned} a &= -(A^2 + AE + F) \\ b &= -\mu(2AB + BE) \\ c &= -\mu^2 B^2 \end{aligned}$$

whose components A , B , E , and F are constants described by the equations

$$\begin{aligned} A &= \frac{A_1 D_{21} - D_{22} + A_3 D_{23}}{-D_o} \\ B &= \frac{B_1 D_{21} + B_3 D_{23}}{-D_o} \\ E &= -2(\hat{\rho}_2 \cdot \vec{R}_2) \\ F &= R_2^2 \end{aligned}$$

whose components of form D_{2j} and D_o are described in the Method of Gauss, and whose components of A_1 , A_3 , B_1 , and B_3 are themselves described by the following set of equations:

$$A_1 = \frac{\tau_3}{\tau}, A_3 = \frac{-\tau_1}{\tau}, B_1 = \frac{A_1}{6}(\tau^2 - \tau_3^2), B_3 = \frac{A_3}{6}(\tau^2 - \tau_1^2)$$

The roots are then used in the first iteration f and g functions as described above, and the Method is iterated. However, after the first iteration, more accurate f and g functions can be used.

3.4.3 Approximating f and g

Once the first iteration of the Method of Gauss has been completed, and preliminary guesses for the \vec{r}_2 and $\dot{\vec{r}}_2$ vectors have been calculated, f and g values more accurate than the ones provided by the simplified functions must be found. There are two methods of finding more accurate f and g values, both of which are used in this analysis: the Taylor-Series Expansion and the Newton-Raphson Method.

Using a Taylor-series expansion for the vector \vec{r}_i will give a series which can be split into two distinct series formulas: one describing f , and one describing g . The following equation describes the expansion of said \vec{r}_i vector.

$$\vec{r}_i = \vec{r}_2 + \frac{1}{2}\ddot{\vec{r}}_2 \tau_i^2 + \frac{1}{6}\dddot{\vec{r}}_2 \tau_i^3 + \frac{1}{2}\ddot{\vec{r}}_2 \tau_i^2 + \frac{1}{6}\dddot{\vec{r}}_2 \tau_i^3 + \frac{1}{24}\ddot{\vec{r}}_2 \tau_i^4 + \dots$$

where τ_i represents the time intervals in Gaussian units, and the derivatives of \vec{r}_i are defined as follows:

$$\begin{aligned} \ddot{\vec{r}}_2 &= \frac{-\mu \vec{r}_2}{r_2^3} \\ \ddot{\vec{r}}_2 &= 6 \frac{\mu(\vec{r}_2 \cdot \vec{r}_2)}{2r_2^5} \vec{r}_2 - \frac{\mu}{r_2^3} \dot{\vec{r}}_2 \\ \ddot{\vec{r}}_2 &= (3uq - 15uz^2 + u^2)\vec{r}_2 + 6uz\dot{\vec{r}}_2 \\ u &= \frac{\mu}{r_2^3} \quad z = \frac{\vec{r}_2 \cdot \dot{\vec{r}}_2}{r_2^2} \quad q = \frac{\dot{\vec{r}}_2 \cdot \dot{\vec{r}}_2}{r_2^2} - u \end{aligned}$$

As seen above, higher degree Taylor polynomials can be used to obtain precise values that depend on numerical values for \vec{r}_2 and $\dot{\vec{r}}_2$. These values are then perfected with each iteration and inserted back into the Taylor polynomials to get more accurate answers.

When using Taylor-series f and g functions, each iteration begins with calculations of new f and g functions, where f characterizes the r value whereas g characterizes the τ value as shown in the equations below.

$$f_i = 1 - \frac{\mu \vec{r}_2}{r_2^3} \tau_i^2 + \frac{\mu (\vec{r}_2 \cdot \dot{\vec{r}}_2)}{2r_2^5} \tau_i^3 + \frac{1}{24} (3uq - 15uz^2 + u^2) \tau_i^4$$

$$g_i = \tau_i - \frac{\mu}{6r_2^3} \tau_i^3 + \frac{1}{24} 6uz \tau_i^4$$

Another method of determining the f and g functions can be found using the definitions of the f and g functions [7]. If the semi-major axis and eccentricity are known (and these values can be calculated after the first iteration), then f and g can be described by the equations

$$f = 1 - \frac{a}{r^2} (1 - \cos \Delta E)$$

$$g = \tau - \frac{1}{n} (\sin \Delta E - \Delta E)$$

where n is the mean motion, the angular speed required for a body to complete one circular orbit at constant velocity and equal to $\frac{k}{\sqrt{a^3}}$. ΔE is equal to $E - E_2$, where E is the eccentric anomaly. Eccentric anomaly is defined in Kepler's Equation, which states that

$$M = E - e \sin E$$

E can be found by iteration via the Newton-Raphson method of finding the roots of a function (hence the name of the method for finding f and g). By this method, the following equations [9] are iterated until the difference between x_{n+1} and x_n is sufficiently small, and where x represents the guesses of the eccentric anomaly. The functions for determining these guesses are as follows:

$$x_{n+1} = x_n - \frac{f(x)}{f'(x)}$$

$$f(x) = x - EC \sin x + ES(1 - \cos x) - n\Delta t$$

$$f'(x) = 1 - EC \cos x + ES \sin x$$

where, according to Danby [9],

$$EC = e \cos(E_2) = 1 - r_2/a$$

$$ES = e \sin(E_2) = u/na^2$$

where n is mean motion as before, a is the semi-major axis of the orbit, e is eccentricity of the orbit, and u is $\vec{r}_2 \cdot \dot{\vec{r}}_2$.

The starting value for the iterations of the Newton-Raphson method in this case can be simplified to $n\Delta T$ at low eccentricities [7]. However, it cannot be assumed that that is always the case. As such, there is a more complete formula [9] used to determine a starting value when $e > 0.10$. This formula is given as

$$x_o = n\Delta t + \sigma k e - ES$$

where k is not the Gaussian constant, but rather a value falling within the bounds $0 \leq k \leq 1$, and σ is a representation of the sign (either positive or negative) of the expression

$$\frac{1}{e}(ES \cos(n\Delta t - ES) + EC \sin(n\Delta t - ES))$$

where EC and ES are defined as previously. By iterating the Newton-Raphson method to find a ΔE for each observation, f and g values can be calculated from their respective functions.

These new approximations for f and g that now depend on \vec{r}_2 and $\dot{\vec{r}}_2$ can be plugged into all of the equations of the Method of Gauss to get more accurate values for \vec{r}_2 and $\dot{\vec{r}}_2$. Because changing \vec{r}_2 and $\dot{\vec{r}}_2$ changes ρ values, corrections for light travel time must also be updated for each iteration, correcting the time such that the new time is equivalent to $\frac{\rho_i}{c}$ subtracted from the time of observation. This means that each iteration is dependent upon the newly calculated \vec{r}_2 , $\dot{\vec{r}}_2$, and τ values. Iteration of the Method of Gauss ends when differences in r_2 values between iterations reach a desired tolerance and cease changing to a satisfactory decimal place. For the purposes of this experiment, a tolerance of $1e-13$ was used for Taylor expansion, and a tolerance of $1e-19$ for the Newton-Raphson method.

3.4.4 Calculated Orbital Elements

After the values of the asteroid's orbital elements were determined, the differing methods in achieving the resultant values were analyzed. Thus, in the following tables, Models 1 and 2 represent data determined using iterations of a Taylor polynomial whereas Model 3 represents data found using Newton-Raphson iterations. Moreover, the permutations represent combinations of three of the four observation sessions with the first and fourth observations constant to maximize a time baseline for the observations.

Table 4: The Calculated Orbital Elements from the Method of Gauss

Model	Permutation	Method	a (AU)	e	i (°)	Ω (°)	ω (°)	M (°)	*P (yr)
1	1,2,4	Taylor (4th Order)	1.464	.377	23.819	221.549	319.452	56.245	1.770
1	1,3,4	Taylor (...)	1.629	.434	25.128	219.809	324.119	46.338	2.080
2	1,2,4	Taylor (...)	1.436	.366	23.521	221.853	318.536	58.312	1.721
2	1,3,4	Taylor (...)	1.695	.454	25.511	219.184	325.618	43.249	2.206
3	1,2,4	Newton-Raphson	1.517	.397	24.312	220.974	321.083	52.669	1.869
3	1,3,4	Newton-Raphson	1.497	.390	24.159	221.260	320.329	53.997	1.834

* Denotes calculated values other than the main 6 orbital elements

As shown above, not only did the data vary in the iteration methods used during the Method of Gauss calculations, but permutations were also conducted between the four observations of the asteroid.

Table 5: The Calculated Orbital Elements from the Method of Gauss (Averaged)

Model	Permutation	Method	a (AU)	e	i (°)	Ω (°)	ω (°)	M (°)	*P (yr)
1	Average	Taylor (4th Order)	1.547	.406	24.474	220.679	321.786	51.955	1.926
2	Average	Taylor (...)	1.565	.410	24.516	220.518	322.077	50.780	1.964
3	Average	Newton-Raphson	1.508	.394	24.236	221.117	320.706	53.333	1.851
JPL	N/A	N/A	1.542	.406	24.526	220.745	321.737	51.154	1.916

* Denotes calculated values other than the main 6 orbital elements

For the Taylor series, while the {1,2,4} permutation generally provided underestimates of the orbital elements (with the exception of the longitude of the ascending node and the mean anomaly), the {1,3,4} generally resulted in overestimates of the orbital elements. While the difference between the two different permutations was pretty significant for the Taylor series iterations, there was minimal difference between the two permutations for the Newton-Raphson iterations. However, the averaged values of the orbital elements determined using Taylor series resulted in similar values when compared to values determined using Newton-Raphson iterations.

Additionally, in comparison with the predictions of the orbital elements' values from JPL Horizons, a small-body database, the Taylor series' values alone varied greatly compared to the values determined using Newton-Raphson iterations. However, when the averages of the permutations were taken, the Taylor series values were significantly closer to the JPL Horizons' values for the orbital elements of 1998 OH, implying that the Taylor series method results in orbital elements approximately evenly spaced about the actual values while Newton-Raphson more closely converges on individual permutations. In conclusion, the orbital elements determined using Taylor series iterations relied more on the independent permutations themselves whereas the Newton-Raphson method seems more adaptable to the different permutations of the observational data.

Another way in which we assessed the accuracy of the calculated orbital elements was by using them to calculate the right ascension and declination of 1998 OH that the another team obtained during their observations [10]. Because the Taylor series' orbital elements significantly varied with each permutation, the Newton-Raphson method's calculated orbital elements were used to determine a set of predicted positional data (Table 6). The right ascension of these predictions and observations matched, with one notable exception for the 23rd of June, to within one arcsecond, and the declination of these predictions and observations matched with one notable exception for the 23rd of June, to within five arcseconds consistently, thus implying validity in the data processing and thus, accuracy of the orbital elements.

However, the sheer magnitude of the variation on the June 23rd date calls into question the accuracy of the ephemeris generated by the predicted orbital elements. When considering the significant difference between the JPL Horizons database value for a and the Newton-Raphson calculation for that same value, it should be noted that such a difference in orbital elements has the potential to explain the discrepancy for that data point.

Furthermore, using the orbital elements calculated by Newton-Raphson, the class of the asteroid can be calculated. Because the semi-major axis is greater than the Earth's semi-major axis of 1 AU and the calculated perihelion of 1998 OH (.9 AU) is less than the aphelion of the Earth (1.017AU) [7], 1998 OH

Table 6: Assessing the Accuracy of the Orbital Elements

Date (UTC)	Observed α	Observed δ	Predicted α	Predicted δ
June 19th, 2019 06:05:45.900	14:32:03.55	+37:44:35.9	14:32:03.73	+37:44:29.26
June 23rd, 2019 06:20:04.289	14:48:05.24	+36:25:21.3	14:48:34.63	36:19:23.88
July 05th, 2019 07:34:01.140	15:25:08.02	+32:13:11.72	15:25:08.27	+32:13:11.72
July 10th, 2019 07:28:03.839	15:37:30.39	+30:26:15.6	15:37:30.69	+30:26:19.77

was determined to fall into the Apollo class of asteroids. Apollos are Earth crossing asteroids, having a perihelion less than or equal to Earth's aphelion and a semi-major axis greater than the Earth ($a > 1$ AU)

3.5 Differential Correction

With four total observations of 1998 OH, differential correction was conducted in attempt to improve the positional and velocity vectors of the asteroid, and thus, its orbital elements. Using this method, multiple linear regressions were conducted in attempt to reduce the deviations of the six Cartesian components of the positional and velocity vectors.

To calculate the changes in the components of \vec{r}_2 and $\dot{\vec{r}}_2$, the inverse of a Jacobian matrix containing the sums of products of right ascension and declination from each of the four observations was used, as shown in the equation below.

$$\begin{pmatrix} \Delta\alpha_i \frac{\partial\alpha_i}{\partial x} \\ \Delta\alpha_i \frac{\partial\alpha_i}{\partial y} \\ \Delta\alpha_i \frac{\partial\alpha_i}{\partial z} \\ \Delta\alpha_i \frac{\partial\alpha_i}{\partial \dot{x}} \\ \Delta\alpha_i \frac{\partial\alpha_i}{\partial \dot{y}} \\ \Delta\alpha_i \frac{\partial\alpha_i}{\partial \dot{z}} \end{pmatrix} = \begin{pmatrix} \frac{\partial\alpha}{\partial x} \frac{\partial\alpha}{\partial x} & \frac{\partial\alpha}{\partial x} \frac{\partial\alpha}{\partial y} & \frac{\partial\alpha}{\partial x} \frac{\partial\alpha}{\partial z} & \frac{\partial\alpha}{\partial x} \frac{\partial\alpha}{\partial \dot{x}} & \frac{\partial\alpha}{\partial x} \frac{\partial\alpha}{\partial \dot{y}} & \frac{\partial\alpha}{\partial x} \frac{\partial\alpha}{\partial \dot{z}} \\ \frac{\partial\alpha}{\partial y} \frac{\partial\alpha}{\partial x} & \frac{\partial\alpha}{\partial y} \frac{\partial\alpha}{\partial y} & \frac{\partial\alpha}{\partial y} \frac{\partial\alpha}{\partial z} & \frac{\partial\alpha}{\partial y} \frac{\partial\alpha}{\partial \dot{x}} & \frac{\partial\alpha}{\partial y} \frac{\partial\alpha}{\partial \dot{y}} & \frac{\partial\alpha}{\partial y} \frac{\partial\alpha}{\partial \dot{z}} \\ \frac{\partial\alpha}{\partial z} \frac{\partial\alpha}{\partial x} & \frac{\partial\alpha}{\partial z} \frac{\partial\alpha}{\partial y} & \frac{\partial\alpha}{\partial z} \frac{\partial\alpha}{\partial z} & \frac{\partial\alpha}{\partial z} \frac{\partial\alpha}{\partial \dot{x}} & \frac{\partial\alpha}{\partial z} \frac{\partial\alpha}{\partial \dot{y}} & \frac{\partial\alpha}{\partial z} \frac{\partial\alpha}{\partial \dot{z}} \\ \frac{\partial\alpha}{\partial \dot{x}} \frac{\partial\alpha}{\partial x} & \frac{\partial\alpha}{\partial \dot{x}} \frac{\partial\alpha}{\partial y} & \frac{\partial\alpha}{\partial \dot{x}} \frac{\partial\alpha}{\partial z} & \frac{\partial\alpha}{\partial \dot{x}} \frac{\partial\alpha}{\partial \dot{x}} & \frac{\partial\alpha}{\partial \dot{x}} \frac{\partial\alpha}{\partial \dot{y}} & \frac{\partial\alpha}{\partial \dot{x}} \frac{\partial\alpha}{\partial \dot{z}} \\ \frac{\partial\alpha}{\partial \dot{y}} \frac{\partial\alpha}{\partial x} & \frac{\partial\alpha}{\partial \dot{y}} \frac{\partial\alpha}{\partial y} & \frac{\partial\alpha}{\partial \dot{y}} \frac{\partial\alpha}{\partial z} & \frac{\partial\alpha}{\partial \dot{y}} \frac{\partial\alpha}{\partial \dot{x}} & \frac{\partial\alpha}{\partial \dot{y}} \frac{\partial\alpha}{\partial \dot{y}} & \frac{\partial\alpha}{\partial \dot{y}} \frac{\partial\alpha}{\partial \dot{z}} \\ \frac{\partial\alpha}{\partial \dot{z}} \frac{\partial\alpha}{\partial x} & \frac{\partial\alpha}{\partial \dot{z}} \frac{\partial\alpha}{\partial y} & \frac{\partial\alpha}{\partial \dot{z}} \frac{\partial\alpha}{\partial z} & \frac{\partial\alpha}{\partial \dot{z}} \frac{\partial\alpha}{\partial \dot{x}} & \frac{\partial\alpha}{\partial \dot{z}} \frac{\partial\alpha}{\partial \dot{y}} & \frac{\partial\alpha}{\partial \dot{z}} \frac{\partial\alpha}{\partial \dot{z}} \end{pmatrix} \begin{pmatrix} \Delta x \\ \Delta y \\ \Delta z \\ \Delta \dot{x} \\ \Delta \dot{y} \\ \Delta \dot{z} \end{pmatrix}$$

For simplicity, the matrix equation above can also be represented by the equation below:

$$a = Jx$$

While the matrix above only contains the variable α for right ascension, the variable implies all positional data, including partial derivatives of the declination (in the matrix and in the subsequent equations). Therefore, in the matrix above, the summations $i = 1$ to $i = n$ are implied for matrices a and J , where n is the number of positional arguments (right ascension and declination). Because only four observations of 1998 OH were conducted, the value of n was eight.

In terms of determining the $\Delta\alpha$ and the partial derivatives in the equations above, further calculations are necessary. While the equation for the former is just $\Delta\alpha = \alpha_{obs} - \alpha_{fit}$ where α_{obs} is the observational positional data obtained using astrometry and α_{fit} denotes the calculated positional data obtained by running the orbital elements generated from the Method of Gauss through an ephemeris generator. On the other hand, the partial derivatives must be determined numerically, where Δ was assigned the value of $1e - 4$ as suggested by Danby [9]. Additionally, the $x, y, z, \dot{x}, \dot{y}, \dot{z}$ terms represent the positional

elements of the \vec{r}_2 and $\dot{\vec{r}}_2$ values determined from the Method of Gauss.

$$\frac{\partial \alpha_i}{\partial x} = \frac{\alpha_i(x + \Delta, y, z, \dot{x}, \dot{y}, \dot{z}) - \alpha_i(x - \Delta, y, z, \dot{x}, \dot{y}, \dot{z})}{2\Delta}$$

Therefore, to find the changes in the positional and velocity vectors, the pseudo inverse of J is taken and multiplied by a , as shown in the equation below.

$$J^{-1}a = x$$

In terms of determining whether the differential correction improved the orbital elements, the deviation value (RMS) of the positional data before and after differential correction was determined using the subsequent equation. To determine the new fit positional data, the altered positional and velocity vectors were, again, run through the ephemeris generator to determine new right ascension and declination values.

$$RMS_{orbit} = \sqrt{\frac{\sum (\alpha_{obs} - \alpha_{fit})^2}{n - 6}}$$

After calculating the RMS values for the orbital elements determined using Newton-Raphson iterations, it was concluded that while it didn't significantly improve the first permutation of orbital elements, the RMS value was lower for the second permutation and thus, slightly improved the accuracy of the orbital elements as shown in Table 7.

Table 7: Differential Correction Effects on Orbital Elements for the Second Permutation of Newton Raphson

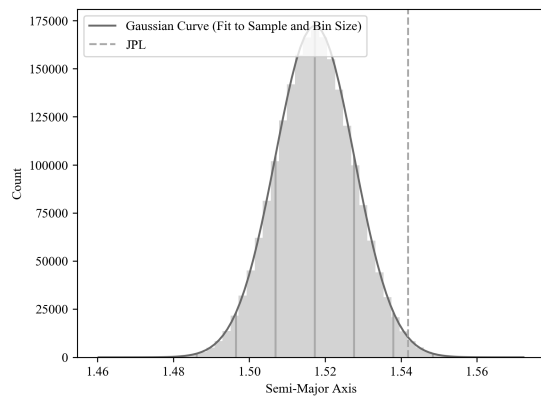
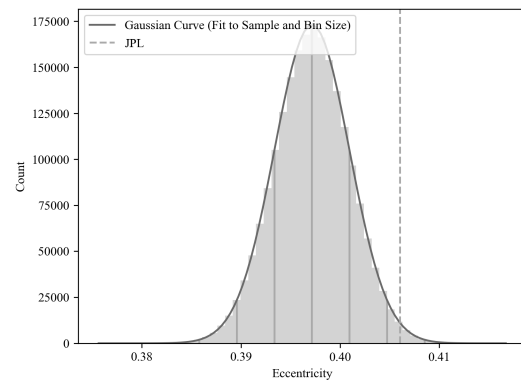
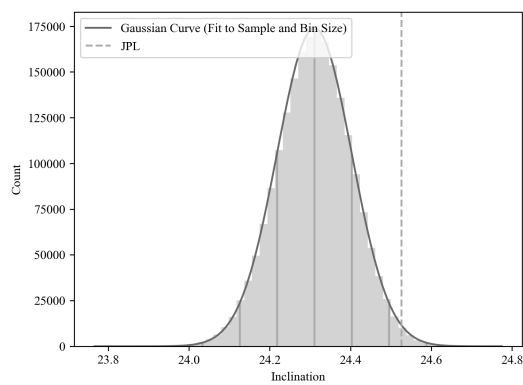
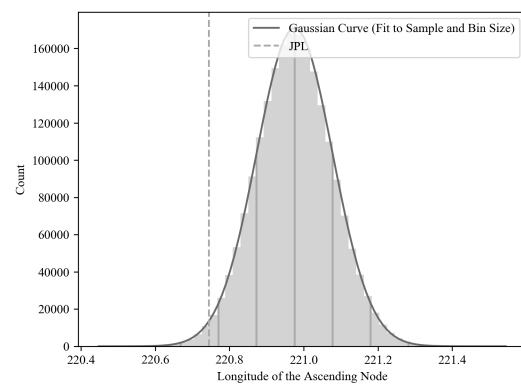
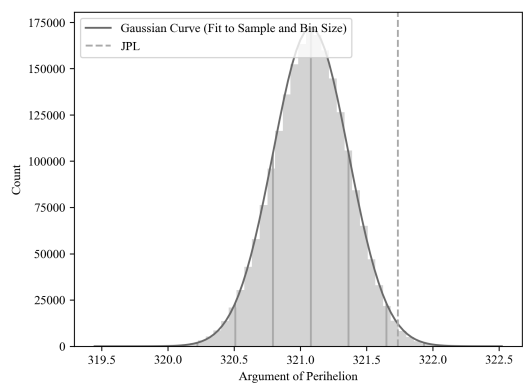
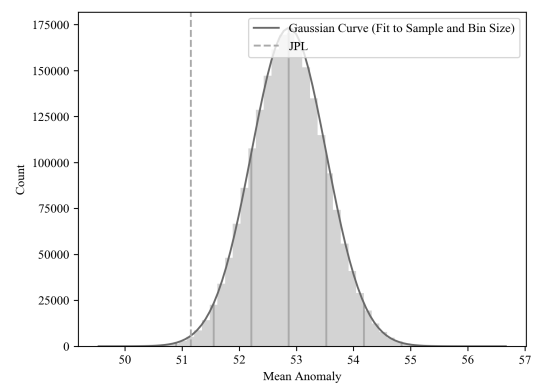
	a (AU)	e	i (°)	Ω (°)	ω (°)	M (°)	*P (yr)
No Differential Correction	1.497	.390	24.159	221.260	320.329	53.997	1.834
Differential Correction	1.498	.390	24.147	221.197	320.481	53.906	1.834

Nevertheless, the decreased deviations between the positional data from the differential correction should have improved the accuracy of the elements. For the values calculated using the Taylor series, however, the difference between the RMS values was negligible, and thus, would not have resulted in a significantly improved orbit.

3.6 Monte Carlo Simulation Results

After completing differential equations on the positional and velocity vectors in attempt to improve the calculated orbital elements, the uncertainties on the right ascension and declination of the asteroid from the astrometry calculations were then used to generate a range of random input coordinates for the Method of Gauss in a series of Monte Carlo simulations.

In a Monte Carlo simulation, the input value or values are varied randomly, but along a weighted distribution which corresponds to a Gaussian normal distribution. For an input variable, the normal distribution is defined with its midpoint being at the input value, and one standard deviation on the normal distribution is equal to the input uncertainty. These slightly varied values are then input into the functions used; in this case, the values are inputted into the Method of Gauss and then slightly varied orbital elements are returned. As the number of iterations for the Monte Carlo simulation increases,

(a) Semi-Major Axis (a)(b) Eccentricity (e)(c) Orbit Inclination (i)(d) Longitude of Ascending Node (Ω)(e) Argument of Perihelion (ω)(f) Mean Anomaly (M)**Figure 3:** Results of the Monte Carlo Simulations to Determine the Orbital Elements' Uncertainties

the outputs should approximate a normal curve in their placement. This is represented by a number of histograms, each composed of 48 bins.

For this experiment, the Monte Carlo uncertainty simulation was done using the Method of Gauss with the Newton-Raphson f and g determination method due to the inconsistency in the values generated using the Taylor series such that the predicted JPL value would not have fallen within three standard deviations, and all values were corrected differentially. 2,084,388 iterations were run, with each returning a value for each orbital element. When the distribution formed by these variations was compared against the predicted values of the JPL Horizons database, however, the JPL Horizons orbital elements were consistently slightly more than two standard deviations away from the mean.

Table 8: Orbital Elements with Standard Deviations

Orbital Element	Mean Element Value	Standard Deviation	JPL Values
a (AU)	1.517	0.010	1.542
e	0.397	0.004	0.406
i ($^{\circ}$)	24.311	0.092	24.526
Ω ($^{\circ}$)	220.975	0.102	220.745
ω ($^{\circ}$)	321.079	0.285	321.737
M ($^{\circ}$)	52.868	0.657	51.154

The orbital elements are fairly uniform, but if the standard deviations are considered in terms of standard deviation per unit of mean element value, the mean anomaly is much less precisely calculated than the other elements. This lack of precision is mirrored in the comparisons between f and g function types and averages.

4 Conclusion

While the Method of Gauss resulted in orbital elements that had relatively low uncertainties, their values consistently deviated from those predicted by the JPL Horizons database at over two standard deviations, and there was a significant error—to the order of several arcminutes—in comparing calculated right ascensions and declinations on the central data point of the observation whose orbital elements were used. There are several points of error that could have resulted in the deviations calculated.

For instance, the inconsistent time periods between the observation sessions and the different quality of data between the first two observation sessions and the last two observation sessions could have resulted in inconsistencies. By the procedure designed, running an orbital determination across the largest interval of time was necessary. However, the observations themselves were not evenly spread across the large interval. Of the four observations, two took place in late June, and two took place in the middle of July. The reason for this gap in observation time is due to cloudy observing conditions. Because the clouds covered the portion of the sky where the asteroid ought to be, they obscured the view of an already dim object, and thus the object was unable to be observed. As the Method of Gauss is limited to three observations and the first and last ones are fixed, there are only two possible permutations; each of which, when run, return only one real positive root, further restricting the possibilities of better orbital determinations. Additionally, the Taylor method is shown to be significantly influenced by the composition of each permutation - thus more observations and more evenly spaced observations would likely

minimize the error shown.

Because the sky was partially cloudy on the third and especially the fourth night, the resulting decrease in quality of those images could have influenced the data taken. Furthermore, the small sample size of observations relatively close to each other could have magnified any small deviations, especially if those deviations occurred on a more obscured night. The fourth observation fits the potential for these criteria to be fulfilled, and thus any inconsistency may have spread through the entire analysis. Another source of error includes the change in exposure time between the first and last two observations as well as the change in filter from visual to clear during the third observation. These inconsistencies when observing 1998 OH can introduce deviations between the sets of data, which the Method of Gauss' lack of flexibility would regurgitate. In addition to observational errors, other sources of error are introduced when processing the data. During data reduction, astrometry, and photometry, different programs were used, and therefore, more error could have been introduced between programs. This error could have carried through to affect the parameters of the Method of Gauss thus decrease the accuracy of calculated orbital elements.

While observational error is the most likely cause of the deviations between the predicted orbital elements and the calculated orbital elements, it is possible, though extremely unlikely, that calculated orbital elements' deviation from those provided by the database JPL Horizons might instead be a result of perturbations within the orbit of 1998 OH.

Many of the errors described above could have been corrected via simple changes to the procedure and the method. If we were to repeat this project, we would begin by observing more often. This would ensure that slight deviations or inconsistencies in data between nights would not skew the results irreparably. Six or seven observations would have provided the ability to run the Method of Gauss on four or more permutations depending on roots given from the Scalar Equation of Lagrange. This would allow for the omission of outliers and the determination of the most accurate combination of positional data.

Additionally, with an increased frequency of observation, even if two data points were too close to be used together, they could have been used to offset the lack of observational data on cloudy nights by choosing to use one that provides more even spacing between observations. Beyond that, the Method of Gauss may have been biased in and of itself. Other orbital determination methods, such as the Method of Laplace, could have been used as comparison and would have served to enhance our results. The use of a single orbital determination method, such as the Method of Gauss, may be useful in some situations, but ultimately restricts results to one perspective.

Acknowledgements

First and foremost, we would like to recognize the academic director of SSP and our dedicated mentor, Dr. Adam Rengstorf, for his tireless work and gracious assistance. We would further like to recognize our other instructors, Dr. William Andersen and Dr. Aaron Bauer, and their essential contributions to the background necessary to complete this orbit determination, including teaching us how to calculate orbital elements and the fundamentals of automating the Method of Gauss in Python, respectively. We would also like to recognize the SSP site director Barbara Martinez for her inexhaustible passion and commitment to the Summer Science Program and its students. We would like to thank the wonderful teaching assistants, Cyndia Cao, Anthony Flores, Descartes Holland, and Emma Loudon for putting their time and energy into giving us this unforgettable experience. We would also like to thank Dr. Dan KlingleSmith, who normally runs Etsorn Observatory, for allowing us to use astronomical equipment which would normally be unobtainable, or at the very least, extremely expensive. By extension we would like to acknowledge the New Mexico Institute of Mining and Technology for hosting us on their campus and for providing room and board, computers, classrooms, and other required resources for this program. Finally, we would like to thank the Summer Science Program and the incredible alumni who have kept it alive with donations for so long, allowing us to undertake this incredible journey.

A 1998 OH MPC Report

The following figure depicts the observational data of 1998 OH that was sent to the International Astronomical Union's Minor Planet Center to be published.

```

COD 719
CON A. W. Rengstorf
CON [adamwr@pnw.edu]
OBS W. E. Finkelstein, R. LoRusso, I. Xu
MEA W. E. Finkelstein, R. LoRusso, I. Xu
TEL 0.36-m f/11 reflector + CCD
NET GAIA DR2
NUM 8
ACK Team 8 - 1998 OH

12538      C2019 06 21.28094 14 40 28.65 37 05 01.1      16.4 V      719
12538      C2019 06 21.28541 14 40 29.84 37 04 55.0      16.5 V      719
12538      C2019 06 26.23986 14 58 32.21 35 24 33.4      16.7 V      719
12538      C2019 06 26.27949 14 58 39.74 35 23 40.8      16.6 V      719
12538      C2019 07 11.22242 15 39 38.74 30 06 47.3      17.2 R      719
12538      C2019 07 11.23709 15 39 40.75 30 06 27.6      17.0 R      719
12538      C2019 07 15.25860 15 48 43.94 28 40 31.6      17.6 V      719
12538      C2019 07 15.28230 15 48 47.01 28 40 01.9      17.4 V      719

```

Figure 4: Data of 1998 OH submitted to the Minor Planet Center

As shown above, two sets of positional coordinates (right ascension and declination) as well as two visual magnitudes of the asteroid for each of the four observations were calculated before submission.

B Analysis and Results of Cloudy Night Experiments

When processing the data, edge effects were avoided by slicing twenty pixels off the edges of all the images before processing them. First, the average pixel values of each set of 11 images was calculated after the bias images were subtracted from the dark images in the first two experiments. Then, when calculating the uncertainty of the signals of the data, the standard deviation between the pixels of an image and its subsequent image was calculated. Then the mean of the standard deviations were taken for each set of eleven images.

$$\sigma = \frac{|x_2 - x_1|}{\sqrt{2}}$$

Using the equation above to calculate the standard deviation of corresponding pixels between each image, the standard error propagation of the data was found and represented by the error bars in the subsequent graphs.

B.1 Dark Current Dependence on Exposure Time

The purpose of this experiment is to test the hypothesis that dark current increases linearly with exposure time. As exposure time increases for any camera, electrons resulting from the greater thermal energy of the system find their way into the potential wells of the CCD chip [11]. These electrons are treated like photons and read out as part of the signal of each pixel. When enough of these electrons accumulate, they result in “dark current noise,” which is usually combated by cooling the CCD chip. The “dark current noise” is an indication of the dark current, so determining a relationship between exposure time and signal gives a relationship between exposure time and dark current.

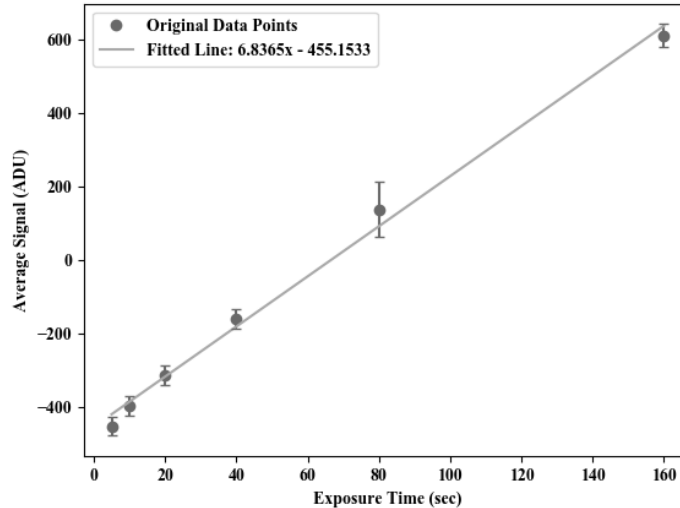


Figure 5: Pixel Counts Dependence on CCD Temperature in Dark Images

To best test the relationship between dark current and exposure time, the temperature of the CCD chip was kept at a constant 22°C – 3°F below the ambient temperature – to ensure that any change in signal was a direct result of a change in dark current. Five series of darks were taken at this constant

temperature with each series at a different exposure time. Exposures began at five seconds and ended at 160 seconds – time was doubled with each series. As mentioned above, a change in signal with a constant chip temperature indicates the presence of dark current. This change in signal is what is hypothesized to increase linearly with exposure time.

After completing the five series, the methods described above in the overview were used to calculate the average signal and error for each set of images. As seen above, when the average signal of each series is graphed with respect to exposure time, a strong linear correlation emerges. This linear relationship between exposure time and signal indicates a linear correlation between exposure time and dark current.

Therefore, even though dark current increases with exposure time, it did not significantly impact image quality when exposure time for 1998 OH was increased from 90 seconds to 120 seconds. This increase proved inconsequential because as part of image processing in AIJ, the effects of dark current are significantly minimized through dark subtraction. If the relationship between dark current and exposure time were exponential, dark subtraction may not work as well for longer exposures and would result in lesser quality images. The fact that the relationship is linear means that it did not noticeably affect images of 1998 OH.

B.2 Dark Current Dependence on CCD Temperature

A second experiment was conducted to determine the relationship between dark current and temperature. In a CCD chip, even when the shutter is closed and there is no incident light, the detectors still register an accumulation of electrical signal. That electrical signal is dark current, caused by a thermal ‘bleed’ from the energy of the system. By decreasing temperature, this active energy is decreased, and thus, dark current is shown to decrease as well. This experiment aims to investigate the relationship between temperature and dark current and to determine the nature of this relationship.

To acquire data for this experiment, the CCD chip was, using a computer-controlled temperature regulator, set to a given temperature and held there throughout the duration of the recording of that set of data. To ensure that other variables did not impact the measurement of dark current, exposure time was kept at a constant 120 degrees, and before each set of data was recorded, there was a period of acclimatization such that the temperature regulator could adjust to the new temperature and hold itself steady there. The temperatures for which data sets were recorded began at 3° C below the ambient temperature—at 22° C—and then for every five degrees celsius below until the temperature regulator could no longer compensate (which occurred at -18° C). For each temperature, a set of five images were taken.

Additionally, the variation in temperature was recorded. These variations are not recorded on the graphs created, but should be considered the deviation possible off the temperature reported. A set of bias frames were taken at $-8 \pm 0.2^\circ \text{C}$, and were median-subtracted from all dark current images. Then, all images were cropped by twenty pixels on all sides, so that irregularities near the edges of the CCD chip would not interfere with the experiment. Based on the assumptions made so far, it is hypothesized that the data collected will be able to be represented through an exponential model. This model ought to be consistent with the Arrhenius law, which states that the rate of a chemical reaction dependent upon temperature is exponential in nature, and is a relation composed of an exponential prefactor and a

Table 9: Fluctuations in the CCD Temperature for Dark Images

Temperature (°C)	Temperature (K)	Uncertainty
-18	255	±0.3
-13	260	±0.3
-8	265	±0.3
-3	270	±0.3
+2	275	±1.0
+7	280	±0.3
+12	285	±0.3
+17	290	±0.3
+22	295	±0.2

temperature-based relationship. The following equation demonstrates this hypothesized Arrhenius law relationship [12], where De_0 is the exponential prefactor, E is the activation energy, T is temperature, and k_B is Boltzmann's constant.

$$De^- = De_0^- * \exp\left(\frac{-\Delta E}{k_B T}\right)$$

The average was taken—along with the associated standard deviation—and plotted as a dependent variable against temperature (in Kelvin). When plotted in such a manner, the data failed to align to a linear relationship. Instead, it appeared to model a relationship more closely adhering to an exponential relationship—as predicted by the Arrhenius Law.

By modeling the dependent variable as the natural logarithm of the dark current signal in electrons, and by modeling the independent variable as one thousand divided by the temperature (in Kelvin), this exponential relationship can be flattened to a linear one and thus analyzed via a linear line of best fit. Such a line for the data consists of a slope of -8972.5206, an intercept of 38.1446, and a Pearson Correlation Coefficient of 0.9971, which indicates a very strong correlation.

As the slope is equivalent to $\frac{-\Delta E}{k_B}$, the E for the entire CCD chip is equal to 0.7733 eV based on the given model, and the exponential prefactor for the entire chip is equal to 38.1446. However, as there are nine sets of images by this experiment, each pixel in the CCD chip can be analyzed separately; with each individual pixel having an exponential prefactor and activation energy, as per Widenhorn's experiment [12]. By conducting a linear regression on each pixel, each will be shown to have differing activation energies and exponential prefactors.

Furthermore, if the Meyer-Neldel Rule holds for this relationship, then there will be a further exponential relationship between the activation energy and the exponential prefactor. This relationship is stated to be equivalent to the following [12]:

$$De_0^- = De_{00}^- * \exp\left(\frac{\Delta E}{E_{MN}}\right)$$

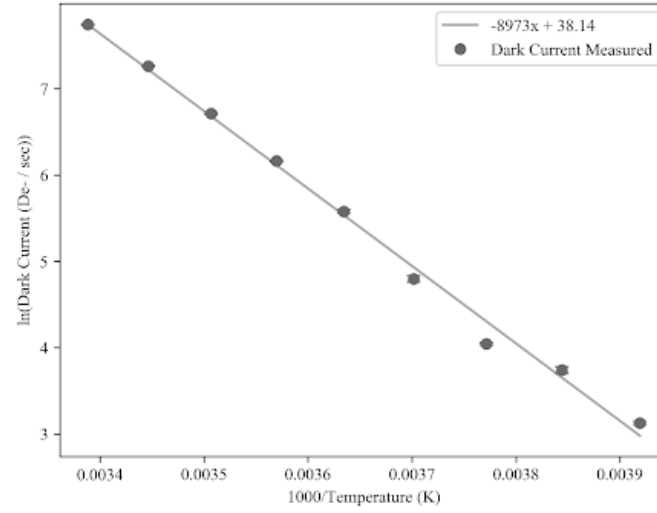


Figure 6: Linear Fit for the Relationship between 1/Temperature and ln(Dark Current)

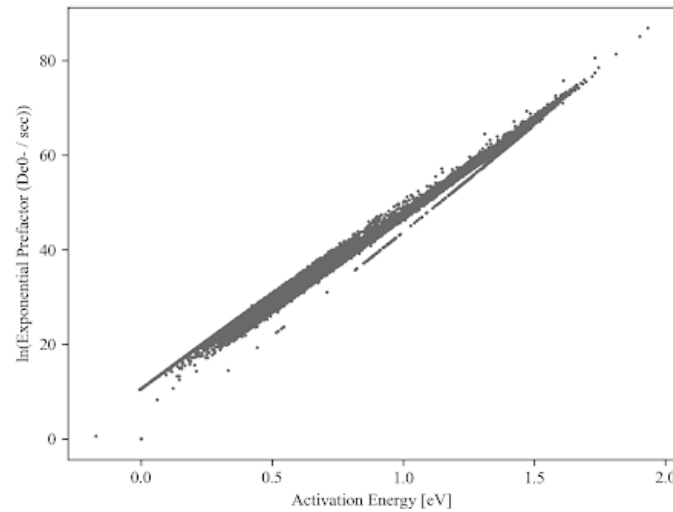


Figure 7: Linear Fit Correlation between Activation Energy and the Exponential Prefactor

Due to the exponential nature of the relationship between dark current and temperature, a single temperature can be found for a given CCD chip where the dark current is no longer dependent upon activation energy. This temperature for a given chip is known as the isokinetic temperature, and is equivalent to $\frac{E_{MN}}{k_B}$. By conducting a linear regression on all 1,103,747 pixels' exponential prefactors and activation energies, the isokinetic temperature can be determined to be 304.1 Kelvins, or about 31°C, well over the maximum temperature to which the CCD was raised.

The exponential nature of the dependence of dark current upon temperature, as shown through this

experiment modeling it to the Arrhenius law means that it is imperative to keep the CCD chip to a cold temperature during observation sessions and while taking darks. This should be done in order to minimize error; because the dark current is exponentially dependent upon temperature, shifting from -10°C to -9.8°C will not cause an appreciable increase in dark current, whereas shifting from 20°C to 20.2°C will. Given that our data for the orbital determination were imaged at a temperature of $-10^{\circ}\text{C} \pm 0.3^{\circ}\text{C}$, the confirmation of an exponential relationship ought not affect our data, but it might matter for future experimentation.

B.3 Bias Level Dependence on CCD Temperature

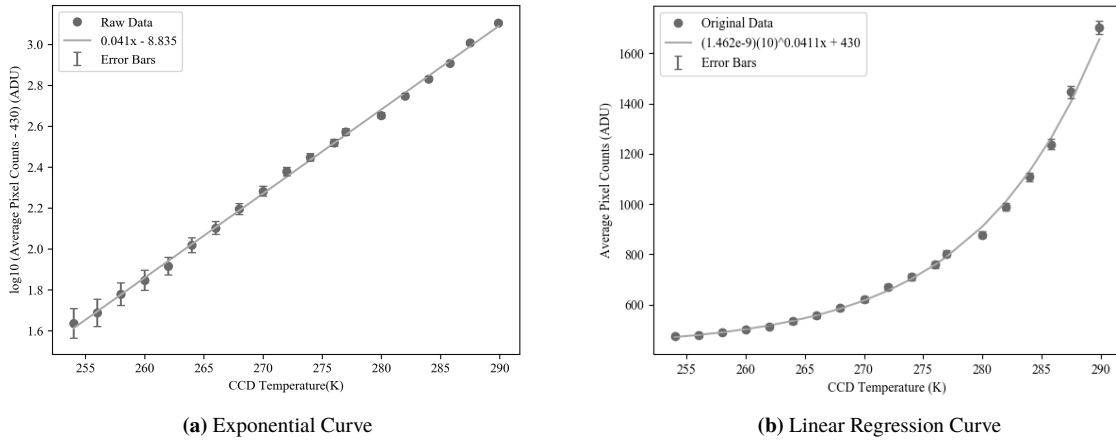


Figure 8: Pixel Counts Dependence on CCD Temperature in Bias Images

In the third cloudy night experiment was conducted to test the hypothesis that bias images are independent of the CCD temperature. If the hypothesis were correct, then the slope of the best fit line would be closer to zero than the uncertainty of the slope. To begin the experiment, the exposure time of standardized to zero seconds (a characteristic of all bias images) and 11 images were taken with each change in CCD temperature. Starting three degrees below the ambient temperature of 24°C , the CCD temperature was decreased by 2°C with every set of 11 images that were taken. Data was then collected until the chip's power reached 100% at 19°C .

Using the data analysis method described at the beginning of Appendix B, the raw data was plotted, which suggested an exponential relationship between CCD temperature and the average signal of bias images. Thus, to support this claim, the linear regression of the data was graphed (Figure 1(a)) to calculate the exponential curve. First, taking a general exponential function,

$$y = a(10)^{kx} + b$$

the y-intercept was subtracted from the right and then the log of all the terms in the function were taken. The function

$$\log_{10}(y - b) = kx + \log_{10}(a)$$

now represents a linear equation that's graphed in Figure 1(a) which a R^2 of .998767, which suggests a

high correlation between the CCD temperature and the average signal in bias images. Additionally, the slope of 0.041 and slope standard deviation of 0.0 (rounded to the nearest thousandth) further counters the hypothesis that CCD temperature and bias images are independent since the average pixel count of bias images increases as the CCD temperature increases.

In consideration of the error calculations, because the average pixel count values were logged before graphing the linear regression, the standard deviations were also logged and subsequently divided by ten to the power of the logged average pixel values from that image set. These errors are represented by the error bars in Figure 9(a). Therefore, to confirm the claim that the curve fit is exponential, the linear function was essentially delogged, resulting in an exponential function that accurately fit the curve of the raw data (Figure 9(b)). Thus, not only was the hypothesis that bias images are independent of CCD temperature disproven, but the relationship between the two variables follow an exponential relationship.

While the initial hypothesis was wrong, the conclusions of this cloudy night experiment doesn't affect the data because the CCD temperature was maintained at the constant temperature of -10°C for all the images. Therefore, the minimal changes in CCD temperatures will standardize the bias images. While the raw data accurately follow an exponential function, the error in the data may be due to the small temperature fluctuations of the CCD chip during the data collection, as shown in Table 10.

Table 10: Fluctuations in the CCD Temperature for Bias Images

Temperature ($^{\circ}\text{C}$)	Temperature (K)	Uncertainty
-19	254	± 0.5
-17	256	± 0.4
-15	258	± 0.2
-13	260	± 0.3
-11	262	± 0.9
-9	264	± 0.6
-7	266	± 0.3
-5	268	± 0.2
-3	270	± 0.3
-1	272	± 0.1
+1	274	± 0.0
+3	276	± 0.3
+4	277	± 0.4
+7	280	± 1.0
+9	282	± 0.3
+11	284	± 0.2
+12.8	285.8	± 0.2
+14.5	287.5	± 0.5
+16.9	289.9	± 0.2

Additionally, the correlation between the CCD temperature and the average pixel values of the bias images is only accurate to the temperatures tested during the experiment because as the CCD temperature approaches zero degrees celcius, the lack of electron movement would reduce the average signal to values that approach zero, which the exponential function with a y-intercept of 430 ADU does not accurately predict.

References

- [1] “Discovery circumstances: Numbered minor planets (10001)-(15000).” Minor Planet Center database, MAY 2019.
- [2] A. Gunn, “How many potentially hazardous asteroids are there?.” <https://www.sciencefocus.com/space/how-many-potentially-hazardous-asteroids-are-there/>, Feb 2019. Accessed on 2019-20-2019.
- [3] “Near-earth object basics.” https://cneos.jpl.nasa.gov/about/neo_groups.html. Accessed on 2019-20-2019.
- [4] D. Byrd, “Today in science: The chelyabinsk meteor.” <https://earthsky.org/space/meteor-asteroid-chelyabinsk-russia-feb-15-2013>, Feb 2019. Accessed on 2019-20-2019.
- [5] H. Weitering, “Nasa reveals new plan to stop asteroids before they hit earth.” <https://www.nbcnews.com/mach/science/nasa-reveals-new-plan-stop-asteroids-they-hit-earth-ncna885316>, June 2018. Accessed on 2019-20-2019.
- [6] B. D. J. Tennenbaum, “How gauss determined the orbit of ceres,” *The American Almanac*, pp. 20–21. Accessed on 2019-20-2019.
- [7] A. W. Rengstorf, “Lecture notes.”.
- [8] A. W. Rengstorf, “Orbit determination packet.”.
- [9] J. M. A. Danby, *Fundamentals of Quantum Mechanics*. Willmann-Bell, 2 ed., 1992.
- [10] S. T. H. Butler, K. Kang, “Observational data.”.
- [11] “Dark current.” <https://www.photometrics.com/resources/learningzone/darkcurrent>. Accessed on 2019-20-2019.
- [12] R. W. et al., “Temperature dependence of dark current in a ccd,” in *Proc. SPIE 4669*, pp. 193–201, 2002.